IEEE Open Journal of the
Industrial Electronics Society

Received 9 August 2022; revised 13 September 2022; accepted 21 September 2022. Date of publication 26 September 2022; date of current version 5 October 2022. The review of this paper was arranged by Associate Editor Giampaolo Buticchi.

Digital Object Identifier 10.1109/OJIES.2022.3209471

Hybrid Switching of Four-Voltage-Vector Model-Free Predictive Current Control for Four-Switch Three-Phase Inverter-Fed SynRM Drive Systems

CHENG-KAI LIN [1] AND CRESTIAN A. AGUSTIN [2]

[1]Department of Electrical Engineering, National Taiwan Ocean University, Keelung 20224, Taiwan
[2]Department of Electrical Engineering, Isabela State University Ilagan Campus, Ilagan 3300, Philippines

CORRESPONDING AUTHOR: CHENG-KAI LIN (e-mail: cklin@mail.ntou.edu.tw)

This work was supported by the National Science and Technology Council, Taiwan under Grant NSTC-111-2221-E-019-025.

ABSTRACT Conventional model-based predictive current control suffers from the common drawbacks of high reliance on system model parameters and the use of a single input voltage vector, which result in large pulsating current ripples and prediction errors. In the case of a four-switch three-phase inverter (FSTPI) topology, the implementation of the predictive controller is exacerbated due to the limited number of candidate voltage vectors. This article presents an integrated model-free predictive current control with a hybrid switching mechanism to solve the problem. The proposed method introduces the combined switching mechanism of input voltage vectors with fixed and variable modulations by increasing the number of switching voltage vectors. The four basic voltage vectors generated in the FSTPI create 24 new synthesized voltage vectors through fourfold linear expansions of the space vector plane. The switching durations of input voltage vectors are determined by calculating their optimal duty ratios. As a result, the proposed method improves the prediction accuracy by increasing the iteration calculations of current differences every sampling period. The proposed method, known as the hybrid switching of four-voltage-vector model-free predictive current control, is practically tested *via* simulation and experimental works to evaluate its effectiveness and performance improvement.

INDEX TERMS Four-switch three-phase inverter (FSTPI), four-voltage-vector, hybrid switching control, model-free predictive current control (MFPCC), synchronous reluctance motor (SynRM).

NOMENCLATURE

Abbreviations

SynRM	Synchronous reluctance motor.
IM	Induction motor.
PMSM	Permanent-magnet synchronous motor.
FSTPI	Four-switch three-phase inverter.
FOC	Field-oriented control.
VC	Vector control.
DTC	Direct torque control.
FCS-MPC	Finite set model predictive control.
MPCC	Model predictive current control.
MBPCC	Model-based predictive current control.
MFPCC	Model-free predictive current control.
HS	Hybrid switching.
4VV	Four-voltage-vector.
LUT	Lookup table.

Variables and Parameters

V_1, V_2, V_3, V_4	Basic voltage vectors.
$VV_1, VV_2, \ldots, VV_{24}$	Synthesized voltage vectors.
$SS_1, SS_2, \ldots, SS_{24}$	Equivalent switching modes.
V_a, V_b, V_c, V_d	Vector application sequence (first, second, third, and fourth).
d_a, d_b, d_c, d_d	Duty ratio sequence (first, second, third, and fourth).

$\Delta i_{\alpha,\beta}$	Current difference in the α–β reference frame.
$i^{ref}_{\alpha,\beta}$	Current commanding/reference value.
$i^{p}_{\alpha,\beta}$	Current predicted value.

I. INTRODUCTION

In the past few decades, power converters and motor drive applications have grown exponentially in various industries, such as manufacturing, power generation, and hybrid electric vehicles [1], [2]. Thanks to the rapid development of fast and powerful microcontrollers, industrial electronics has changed the paradigm and become a leading industry for efficiency and increased performance. Today, electric motor drives are among the notable fields that have gained widespread attention in integrating these technological innovations.

The SynRM is the simplest type of synchronous motor owing to its rotor construction, which is made of iron laminations [3]. The design construction is like that of IM [4] and the performance is comparable to that of PMSMs [5]. In addition, the SynRM offers some excellent features, such as rugged and simple structures, no rotor magnetic material or winding, which makes it cost-effective and draws higher efficiency and field-weakening capability [6], [7]. Meanwhile, the FSTPI topology has the advantages of minimal switching losses and fault-tolerant control [8], which are essential to numerous applications, such as motor drives [9], renewable energy systems [10], and active power filters [11].

Various control strategies have been employed for SynRM, including the widely known classical methods of FOC and DTC [12], [13]. The FOC, also known as the VC, is a type of linear controller that generates voltage vectors from a pulsewidth modulator. FOC has the advantage of good steady-state performance but suffers from moderate dynamic responses and stringent tuning requirements, making it more complicated than DTC [14]. On the other hand, the control strategy of DTC is based on selecting the voltage vector from the error signal between the torque and stator hysteresis controller. Comparing these two classical methods, DTC has a more straightforward control design and structure, better fast dynamic characteristics, and does not require a modulator. However, despite the apparent advantages of DTC, its performance deteriorates, particularly at lower speeds, where high pulsating torque and flux ripples are observed [15]. With the recent progress in the development of control technologies, some advanced methods have been proposed for SynRM, such as slide-mode control, FCS-MPC, and fuzzy control. In particular, the FCS-MPC has received significant attention as a viable alternative to motor drive controls and power converters [16], thanks to its intuitive design, quick response, and multivariable approach. The FCS-MPC uses the equivalent discrete-time model of the system to predict the future behavior of the controlled variables, such as current, flux, or torque. The optimal solution for a predictive controller is obtained by solving a constrained finite-horizon optimization control problem *via* the cost function [17]. However, FCS-MPC relies on the accurate representation of the system model. Deviations or mismatches due to operating conditions and environmental factors can result in performance degradation. Moreover, the conventional MPCC applies only a single voltage vector at every sampling period, causing high current ripples and excessive tracking errors under steady-state control [18].

Several methods have been proposed to address the parameter dependency of the MPCC, including the grey prediction scheme [19], online parameter disturbance observer [20], and Lyapunov adaptive control [21], among others. According to Rodriguez et al. [22], the latest advancements in predictive controller strategies have focused on improving performance and efficiency. Recently, Li et al. [23] have proposed an approach that can improve parameter robustness by combining an extended state observer with the deadbeat predictive current control and a zero-voltage vector redistribution strategy. The method yields favorable performance with forecast disturbance error and parameter mismatch but requires complex parameter tuning and adjustment. In [24], a Luenberger-based disturbance observer is proposed that can regulate the flux and inductance sensitivity. However, due to the one-step delay design of the controller, real-time compensation is compromised. Yang et al. [25] also presented an adaptive disturbance observer by setting a broader predefined tolerance limit for inductance mismatch of the motor load. The method has solved high current oscillations but disregards the salient effects of resistance and flux mismatches. A sliding-mode disturbance observer is proposed in [26], owing to its less complex control algorithm to predict stator currents under different mismatch conditions.

The above-mentioned methods [19], [20], [21], [22], [23], [24], [25], [26] have addressed sensitivity to parameter mismatches to some extent, but the root cause remains unsolved—the controllers' dependency on the system model. A direct and more stable solution to system parameter dependency is presented by Fliess and Join [27] using the model-free approach. Lin et al. [28] were the first to conceptualize model-free control in motor drive applications, which later became known as the MFPCC. The scheme uses the conventional single voltage vector with two sampling measurements in each sampling period. Another approach to MFPCC is presented by Zhang et al. [29] using the combined ultralocal model of the system and an extended state observer. Parameter adjustment is less required herein [29]; however, as described by Zhou et al. [18], the conventional use of a single voltage vector remains unsolved, with high current ripples and tracking errors as primary issues. Multiple voltage vectors are integrated into MFPCC by Agustin et al. [30] and Xiong et al. [31], but the switching duration is designed to be fixed, posing problems with ineffective current measurements. Some previously known approaches and concepts of MFPCC are also discussed in [32].

In order to enhance the robustness and current prediction accuracy of the FSTPI-fed SynRM, a novel switching strategy of input voltage vectors is integrated into the MFPCC. The

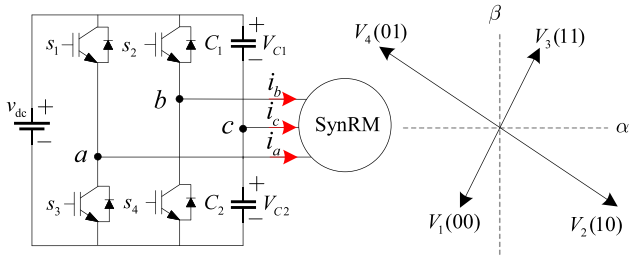

FIGURE 1. Topology of FSTPI-fed SynRM and the corresponding basic voltage vectors V_1, V_2, V_3, and V_4.

method introduces a combined switching mechanism of fixed and variable modulations, known herein as the HS control. The switching controls of input voltage vectors are determined by their optimal duty ratios. Moreover, the number of input voltage vectors is increased by combining four random voltage vectors in every sampling period. However, due to the unique architecture of the FSTPI, the inverter can only generate four basic voltage vectors. Therefore, 24 new synthesized voltage vectors, also known as switching modes, are created by randomly combining four basic voltage vectors. This can be achieved by fourfold linear expansions of the space vector plane. In this article, the proposed control method is termed the HS of 4VV-MFPCC (HS-4VV-MFPCC). The proposed method is expected to improve prediction accuracy by increasing the iterative calculations of current differences every sampling period. Simulation and experimental works are carried out to demonstrate the effectiveness of the proposed HS-4VV-MFPCC using the TMS320F28379D microcontroller.

The rest of this article is organized as follows. An overview of the conventional MBPCC for FSTPI-fed SynRM drive systems is presented in Section II. The principle of HS control and HS-4VV-MFPCC is introduced in Section III and Section IV, respectively Performance validation by simulation is presented in Section V. The detailed experimental works and results are shown in Section VI. Finally, Section VII concludes this article.

II. CONVENTIONAL MBPCC AND MFPCC FOR FSTPI-FED SYNRM

A. FSTPI-FED SYNRM MODEL

The topology of the FSTPI-fed SynRM is shown in Fig. 1, where power switches on the c-phase are replaced by two capacitors, denoted as C_1 and C_2. The remaining two phases have power switches on each leg, denoted by switching states of s_1, s_2, s_3, and s_4. These switching states operate based on the ON and OFF configurations of the power switches. Also shown in the figure is the admissible set of voltage vectors generated by FSTPI with their corresponding switching combinations of $V_1(00)$, $V_2(10)$, $V_3(11)$, and $V_4(01)$.

The mathematical model of the SynRM stator voltage in a two-phase stationary α–β reference frame can be defined [9] as follows:

$$v_x = r_s i_x + L_q \frac{d}{dt}(i_x) + e_x \tag{1}$$

where $v_x = [v_\alpha \ v_\beta]^{\mathrm{T}}$, $i_x = [i_\alpha \ i_\beta]^{\mathrm{T}}$, and $e_x = [e_\alpha \ e_\beta]^{\mathrm{T}}$ are the phase-wise stator voltages, stator currents, and extended back electromotive forces (EMFs), respectively. L_q is the equivalent q-axis inductance and r_s is the stator resistance.

It can be noticed in (1) that the state equation is a first-order system. Hence, the Euler-forward approximation can be used to determine the solution of the differential component as $\frac{d}{dt}(i_x) \approx \frac{i_x(k+1)-i_x(k)}{T_s}$.

Following the discrete-time model of the system in (1), the current prediction equation at $[k+1]$th sampling period can be obtained by

$$i_x^{\mathrm{p}}(k+1) = \frac{L_q - r_s T_s}{L_q} i_x(k) + \frac{T_s}{L_q} v_x(k) + \frac{1}{L_q} e_x(k) \tag{2}$$

where T_s is the sampling time, and superscript "p" indicates the predicted value. Moreover, (2) denotes the prediction equation for the conventional MBPCC.

B. CONVENTIONAL MFPCC

The MFPCC is based on current difference calculations of all admissible candidate voltage vectors generated by the inverter. According to Lin et al. [28], the calculation can be approximated by linear variations between two current measurements using high-precision sensing devices.

The model-free control can be achieved by eliminating the effect of system parameters. As described in [28], the current difference can be calculated as follows:

$$\Delta i_{\alpha,\beta}(k) = i_{\alpha,\beta}(k+1) - i_{\alpha,\beta}(k) \tag{3}$$

where $\Delta i_{\alpha,\beta}(k)$ is the current difference at the $[k]$th sampling period with current measurements of $i_{\alpha,\beta}(k+1)$ and $i_{\alpha,\beta}(k)$. Every candidate voltage vector calculates the current difference component $\Delta i_{\alpha,\beta}(k)$ and stores it in the LUT. In the case of FSTPI, four current differences are available by the end of the sampling instants.

Following the above-mentioned relations, the current prediction defined in (2) can be simplified in the model-free approach as follows:

$$i_{\alpha,\beta}^{\mathrm{p}}(k+1) = i_{\alpha,\beta}(k) + \Delta i_{\alpha,\beta}(k). \tag{4}$$

Similarly, the current prediction at the $[k+2]$th sampling period can be obtained as follows:

$$i_{\alpha,\beta}^{\mathrm{p}}(k+2) = i_{\alpha,\beta}^{\mathrm{p}}(k+1) + \Delta i_{\alpha,\beta}(k+1). \tag{5}$$

The cost function is the optimization criterion in determining the best candidate voltage vector in the next sampling period. It is measured as the square of the absolute value of current errors between predicted and reference values. The cost function can be calculated using the following equation:

$$G = \left| i_{\alpha,\beta}^{ref}(k+2) - i_{\alpha,\beta}^{\mathrm{p}}(k+2) \right|^2. \tag{6}$$

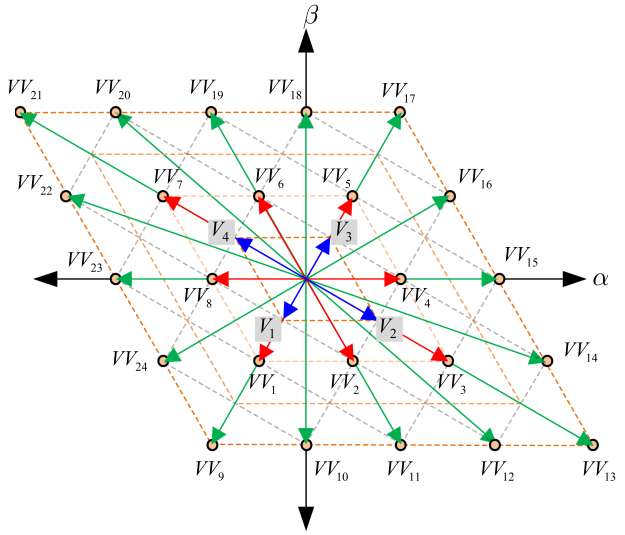

FIGURE 2. Equivalent space voltage vector diagram of the proposed HS-4VV-MFPCC.

III. HS CONTROL

A. SYNTHESIZED VOLTAGE VECTORS

In the case of FSTPI, increasing the candidate voltage vectors is more advantageous as the inverter can only yield four basic voltage vectors, such as V_1, V_2, V_3, and V_4. As depicted in Fig. 2, increasing the candidate voltage vectors in the FSTPI can be obtained in the following two parts: 1) linear combinations of four random basic voltage vectors and 2) expansion of the space vector fourfold. The vector combinations are described as $(V_aV_bV_cV_d)$, such that V_a, V_b, V_c, and V_d represent the proper sequence of the four applied voltage vectors, as first, second, third, and fourth, respectively. The resulting synthesis can generate a total of 256 combinations. However, the control objective of the predictive controller can only select the optimal one from the pool of candidates. As such, with the large selections available for optimization, the complexity of calculations can be compromised. Hence, clustering is enforced to classify all redundant synthesized voltage vectors corresponding to their properties and location in the space vector plane. As shown in Table 1, for instance, the synthesized voltage vector VV_1 can be obtained from 16 possible combinations, such as (1124), (1142) , (3111) , (1131), among others. Despite their unique and varying basic voltage vector compositions, these 16 combinations have the same resultants and can be clustered as a single synthesized voltage vector.

After clustering, 24 distinct combinations are identified and evenly distributed across the space vector plane, as illustrated in Fig. 2. These combinations represent the new candidate switching modes with their corresponding synthesized voltage vectors denoted by the notation of $VV_n, n \in \{1, 2, .., 24\}$. The detailed lists can be seen in Table 1, including their equivalent switching modes and redundant basic voltage vector combinations.

TABLE 1. Clustering of Synthesized Voltage Vectors

Equivalent Switching Mode	Synthesized Voltage vector	Redundant Combination of Basic Voltage Vectors (*) $(V_aV_bV_cV_d),\ a,b,c,d \in \{1,2,3,4\}$
SS_1	VV_1	(1124),(1142),(1214),(1241),(1421),(1412),(2114),(2141),(2411),(4112),(4121),(4211),(1113),(1131),(1311),(3111)
SS_2	VV_2	(1123),(1132),(1213),(1231),(1321),(1312),(2113),(2131),(2311),(3112),(3121),(3211),(1224),(1242),(1422),(2214),(2242),(2124),(2142),(2421),(2412),(4221),(4212),(4122)
SS_3	VV_3	(2224),(2242),(2422),(4222),(2231),(2213),(2123),(2132),(2312),(2321),(3221),(3212),(3122),(1223),(1232),(1322)
SS_4	VV_4	(2234),(2243),(2342),(2324),(2423),(2432),(3224),(3242),(3422),(4223),(4232),(4322),(3221),(3312),(3123),(3132),(3213),(3231),(2331),(2313),(2133),(1332),(1323),(1233)
SS_5	VV_5	(3331),(3313),(3133),(1333),(3324),(3342),(3243),(3234),(3432),(3423),(4332),(4323),(4233),(2334),(2343),(2433)
SS_6	VV_6	(3341),(3314),(3134),(3143),(3413),(3431),(1334),(1343),(1433),(4331),(4313),(4133),(4432),(4423),(4234),(4243),(4324),(4342),(2443),(2434),(2344),(3442),(3424),(3244)
SS_7	VV_7	(4442),(4424),(4244),(2444),(4431),(4413),(4134),(4143),(4314),(4341),(1443),(1434),(1344),(3441),(3414),(3144)
SS_8	VV_8	(4412),(4421),(4124),(4142),(4214),(4241),(1442),(1424),(1244),(2441),(2414),(2144),(1143),(1134),(1341),(1314),(1413),(1431),(3114),(3141),(3411),(4113),(4131),(4311)
SS_9	VV_9	(1111)
SS_{10}	VV_{10}	(1112),(1121),(1211),(2111)
SS_{11}	VV_{11}	(1122),(1212),(1221),(2211),(2221),(2112)
SS_{12}	VV_{12}	(1222),(2122),(2212),(2221)
SS_{13}	VV_{13}	(2222)
SS_{14}	VV_{14}	(2223),(2232),(2322),(3222)
SS_{15}	VV_{15}	(2233),(2323),(2332),(3322),(3332),(3223)
SS_{16}	VV_{16}	(2333),(3233),(3323),(3332)
SS_{17}	VV_{17}	(3333)
SS_{18}	VV_{18}	(3334),(3343),(3433),(4333)
SS_{19}	VV_{19}	(3344),(3443),(4343),(4433),(3434),(4334)
SS_{20}	VV_{20}	(3444),(4344),(4434),(4443)
SS_{21}	VV_{21}	(4444)
SS_{22}	VV_{22}	(4441),(4414),(4144),(1444)
SS_{23}	VV_{23}	(4411),(4141),(4114),(1144),(1414),(1441)
SS_{24}	VV_{24}	(4111),(1411),(1141),(1114)

(*) The numerical combinations represent the subscript order of $(V_aV_bV_cV_d)$.

B. GENERAL HS EQUATION

As mentioned in the previous section, the input sequence of the synthesized voltage vectors is denoted by the following variables: V_a, V_b, V_c, and V_d. In the same way, their corresponding duty ratios are described as d_a, d_b, d_c, and d_d, which hold the identity of

$$d_a + d_b + d_c + d_d = 1 \tag{7}$$

where $d_j = T_j/T_s$, $j \in \{a, b, c, d\}$. The sum of their respective time durations is equal to sampling time, T_s. The expression can be given as follows:

$$T_a + T_b + T_c + T_d = T_s. \tag{8}$$

Following the above-mentioned relations, the general equation of any synthesized voltage vector VV_n can be defined according to the volt-second principle as follows:

$$\begin{cases} VV_n \cdot T_s = T_a \cdot V_a + T_b \cdot V_b + T_c \cdot V_c + T_d \cdot V_d \\ VV_n = d_a \cdot V_a + d_b \cdot V_b + d_c \cdot V_c + d_d \cdot V_d \end{cases} \tag{9}$$

where VV_n refers to any of the candidate synthesized voltage vectors described in Table 1. In implementing the HS mechanism, the duty ratios in (7) need to define based on fixed and variable modulations. The first two input basic voltage vectors are designed to execute at a fixed and equal duty of 25% apiece every sampling period, such that $d_a = d_b = 0.25$. The last two voltage vectors, denoted by d_c and d_d, are in variable durations relative to their calculated optimal duty cycles as $d_c = d_c^{\text{opt}}$ and $d_d = d_d^{\text{opt}}$. The superscript "opt" implies optimal value. From (9), the general HS equation can be obtained relative to their applied switching mode and optimal synthesized voltage vector as follows:

$$VV_x^{\text{opt}} \big| SS_n = 0.25V_a + 0.25V_b + d_c^{\text{opt}} \cdot V_c + d_d^{\text{opt}} \cdot V_d \tag{10}$$

where $x \in \{\alpha, \beta\}$ and $n \in \{1, 2, \ldots\ldots, 24\}$. The selection criteria are defined by minimizing the cost function for every sampling interval. The smallest possible cost value corresponds to the best switching mode or the optimal synthesized voltage vector.

C. HYBRID SWITCHING OF FOUR-VOLTAGE-VECTOR MODEL-BASED PREDICTIVE CURRENT CONTROL

Following the definition of stator voltage in (1), the four input basic voltage vectors of any switching mode can be defined in their model-based form as follows:

$$\begin{cases} V_a = r_s i_x(k,1) + L_q \left(\frac{i_x(k,2) - i_x(k,1)}{T_a} \right) + \hat{e}_x(k-1) \\ V_b = r_s i_x(k,2) + L_q \left(\frac{i_x(k,3) - i_x(k,2)}{T_b} \right) + \hat{e}_x(k-1) \\ V_c = r_s i_x(k,3) + L_q \left(\frac{i_x(k,4) - i_x(k,3)}{T_c} \right) + \hat{e}_x(k-1) \\ V_d = r_s i_x(k,4) + L_q \left(\frac{i_x(k+1,1) - i_x(k,4)}{T_d} \right) + \hat{e}_x(k-1) \end{cases} \tag{11}$$

where (11) is expressed in the $[k]$th sampling period, and variables are described accordingly in Fig. 3. To simplify the equation, the combined action of the four basic voltage vectors, defined in (10), can be considered herein, such that

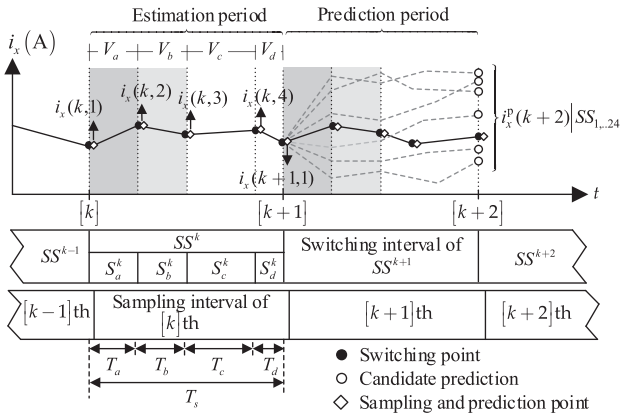

FIGURE 3. Prediction scheme of HS-4VV-MBPCC.

$VV_x|SS_n^k = d_a \cdot V_a + d_b \cdot V_b + d_c \cdot V_c + d_d \cdot V_d$. For instance, between $[k]$th and $[k+1]$th sampling period, the resulting stator voltage equation due to the applied switching mode can be written as follows:

$$VV_x|SS_n^k = r_s i_x(k,1) + L_q \left(\frac{i_x(k+1,1) - i_x(k,1)}{T_s} \right) + \hat{e}_x(k-1) \tag{12}$$

The current measurement in each input basic voltage vector can be derived using (11). From (12), the current prediction at the $[k+1]$th sampling period can be obtained as follows:

$$i_x(k+1,1)|SS_n^k = \left(1 - \frac{r_s T_s}{L_q}\right) i_x(k,1) + \frac{T_s}{L_q} \left(VV_x|SS_n^k - \hat{e}_x(k-1) \right). \tag{13}$$

Extending the prediction horizon to $[k+2]$th sampling instants, the current prediction denoted by superscript "p" can be expressed as follows:

$$i_x^{\text{p}}(k+2)|SS_n^{k+1} = \left(1 - \frac{r_s T_s}{L_q}\right) i_x(k+1,1) + \frac{T_s}{L_q} \left(VV_x|SS_n^{k+1} - \hat{e}_x(k-1) \right). \tag{14}$$

It can be observed in (13) and (14) that the primary component for a model-based predictive controller is the back-EMF. Since there are no direct means to measure its exact value, the back-EMF can be approximated by designing the sampling duration as short as possible. For MPCC, this suggests that variations between adjacent sampling periods can be assumed constant. The relation can be described as follows:

$$\hat{e}_x(k) \approx \hat{e}_x(k-1) = VV_x|SS_n^{k-1} - \frac{L_q}{T_s} i_x(k,1) + \left(r_s - \frac{L_q}{T_s}\right) i_x(k-1,1). \tag{15}$$

Then, the derived equation of back-EMF can be substituted back into (14) to obtain the current prediction equation as follows:

$$\begin{aligned} i_x^{\mathrm{p}}(k+2)\big|\,SS_n^{k+1} &= K_1 \cdot i_x(k-1,1) + K_2 \cdot i_x(k,1) \\ &\quad + K_3 \cdot VV_x|\,SS_n^{k-1} + K_4 \cdot VV_x|\,SS_n^{k} \\ &\quad + K_5 \cdot VV_x|\,SS_n^{k+1} \end{aligned} \tag{16}$$

where constants of parameters K_1, K_2, K_3, K_4, and K_5 are defined accordingly as follows:

$$\begin{cases} K_1 = \frac{-2L_q^2+3L_q r_s T_s - r_s^2 T_s^2}{L_q^2} \\ K_2 = \frac{3L_q^2-3L_q r_s T_s + r_s^2 T_s^2}{L_q^2} \\ K_3 = \frac{-2L_q T_s + r_s T_s^2}{L_q^2} \\ K_4 = \frac{L_q T_s - r_s T_s^2}{L_q^2} \\ K_5 = \frac{T_s}{L_q} \end{cases}. \tag{17}$$

D. MODEL-BASED CALCULATION OF OPTIMAL DUTY RATIOS

Described in (10) is the characteristic of an HS strategy applied to the four input voltage vectors at any given sampling period. The first two applied voltage vectors have fixed duty ratios of 25% each, and the third and fourth applied voltage vectors are modulated according to their optimal duty ratios. By simplifying (10) into a single unknown variable, the equation in $[k+1]$th sampling period can be deduced to

$$\begin{aligned} VV_x|\,SS_n^{k+1} &= 0.25V_a + 0.25V_b + d_c^{k+1} \cdot V_c \\ &\quad + (0.50 - d_c^{k+1}) \cdot V_d \end{aligned} \tag{18}$$

where $0.50 - d_c^{k+1} = d_d^{k+1}$. Similar to the expression defined in (16), (18) can be rewritten as follows:

$$\begin{aligned} i_x^{\mathrm{p}}(k+2)\big|\,SS_n^{k+1} &= K_1 \cdot i_x(k-1,1) + K_2 \cdot i_x(k,1) \\ &\quad + K_3 \cdot VV_x|\,SS_n^{k-1} + K_4 \cdot VV_x|\,SS_n^{k} \\ &\quad + K_5 \cdot (0.25V_a + 0.25V_b + 0.50V_d) \\ &\quad + d_c^{k+1} \cdot K_5 \cdot (V_c - V_d). \end{aligned} \tag{19}$$

It is known that the current prediction in (19) is defined at $[k+2]$th instants. This makes the components $VV_x|SS_n^{k-1}$ and $VV_x|SS_n^{k}$ readily available and obtainable from the previous sampling periods.

The next step is to define the error measure between the current command or reference value and the predicted value. The expression can be obtained as follows:

$$\begin{cases} E_x|\,SS_n^{k+1} = i_x^{\mathrm{ref}} - i_x^{\mathrm{p}}(k+2)\big|\,SS_n^{k+1} \\ = M_x + d_c^{k+1} N_x \end{cases} \tag{20}$$

where new composite variables of M and N in α–β are defined as follows:

$$\begin{cases} M_x = i_x^{\mathrm{ref}} - K_1 \cdot i_x(k-1,1) - K_2 \cdot i_x(k,1) \\ -K_3 \cdot VV_x|\,SS_n^{k-1} - K_4 \cdot VV_x|\,SS_n^{k} \\ -K_5 \cdot (0.25V_a + 0.25V_b + 0.50V_d) \\ N_x = K_5(V_c - V_d) \end{cases}. \tag{21}$$

Finally, the cost function G can be expressed as follows:

$$G|\,SS_n^{k+1} = \left(E_\alpha|\,SS_n^{k+1}\right)^2 + \left(E_\beta|\,SS_n^{k+1}\right)^2. \tag{22}$$

In determining the applicable duty ratios, the resulting cost value is employed *via* partial derivatives of (22), that is $\frac{\partial G}{\partial d_c} = 0$. In this way, one can obtain the following relation:

$$d_c = \left| \frac{-M_\alpha N_\alpha - M_\beta N_\beta}{(N_\alpha)^2 + \left(N_\beta\right)^2} \right| \tag{23}$$

and the duty ratio of the fourth input voltage vector V_d can be calculated simply as follows:

$$d_d = |0.50 - d_c|\,. \tag{24}$$

However, it should be known that the switching duration of the third and fourth input voltage vectors V_c and V_d , respectively, is designed to be variable and adaptive to the calculated duty ratios of (23) and (24). This suggests that the calculated duty ratios may inevitably result in overmodulation. Hence, range constraint solutions are enforced as follows.

1) If $d_c + d_d = 0.50$, the calculated duty ratios are considered optimal, therefore

$$\begin{cases} d_c^{\mathrm{opt}} = d_c \\ d_d^{\mathrm{opt}} = d_d \end{cases}. \tag{25}$$

2) If the first condition satisfies, but the threshold limit $d_c < 0.10$ or $d_d > 0.40$, the optimal duty ratios are recalculated by

$$\begin{cases} d_c^{\mathrm{opt}} = \frac{d_c}{d_c+d_d} \times 50\% \\ d_d^{\mathrm{opt}} = \frac{d_d}{d_c+d_d} \times 50\% \end{cases}. \tag{26}$$

3) If $d_c + d_d < 0.5$ or $d_c + d_d > 0.5$, the same relation established in (26) will be applied.

The working principle of the HS-4VV-MBPCC is summarized in a control block diagram shown in Fig. 4.

IV. HYBRID SWITCHING OF FOUR-VOLTAGE-VECTOR MODEL-FREE PREDICTIVE CURRENT CONTROL

The excellent advantage of MFPCC is that it does not use system parameters for current predictions. It employs a practical and effective approach to measuring current samplings from sensing devices and stores them in the LUT. However, the accuracy obtained from current samples is critical for this current controller. Control performance relies primarily on the stored stator current data in the LUT, and it begins to deteriorate when the current data become obsolete. From (4), it can be observed that the MFPCC involves two types of current data: the actual current samples due to the input basic

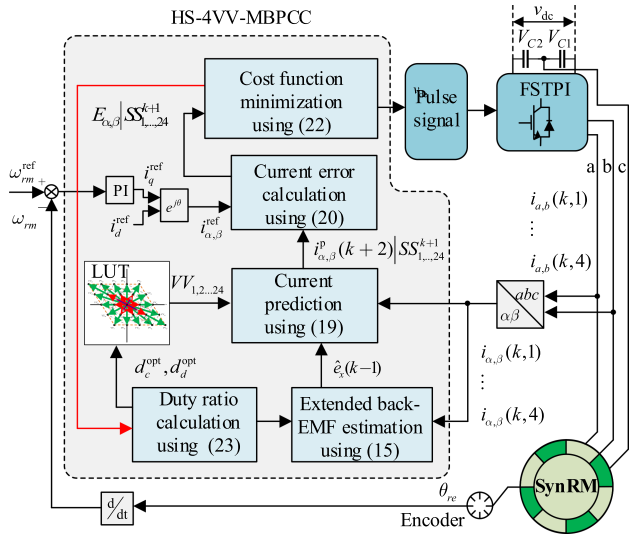

FIGURE 4. Control diagram of HS-4VV-MBPCC.

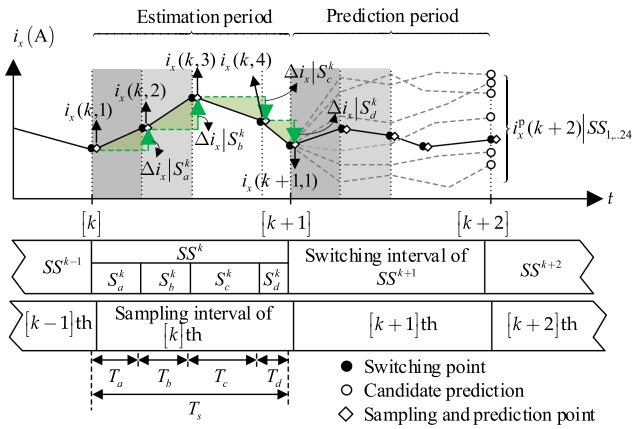

FIGURE 5. Prediction scheme of HS-4VV-MFPCC.

voltage vectors and the current difference calculated between two adjacent current samplings.

To ensure that current data are up to date, the strategy of HS-4VV-MFPCC introduces four current sampling iterations in every sampling interval. As illustrated in Fig. 5, the current samplings at the $[k]$th sampling period are denoted by $i_x(k,1)$, $i_x(k,2)$, $i_x(k,3)$, and $i_x(k,4)$, representing the four input basic voltage vectors, respectively. The current differences, which are defined as the current variation between two adjacent measuring points, are denoted by $\Delta i_x|S_a^k$, $\Delta i_x|S_b^k$, $\Delta i_x|S_c^k$, and $\Delta i_x|S_d^k$. The variables S_a^k, S_b^k, S_c^k, and S_d^k correspond to any of the applied basic voltage vectors at $[k]$th instants, such that $S_a^k, S_b^k, S_c^k, S_d^k \in \{S_1, S_2, S_3, S_4\}$. The four current differences due to their corresponding switching states are defined as follows:

$$\begin{cases} \Delta i_x|S_a^k = i_x(k,2) - i_x(k,1) \\ \Delta i_x|S_b^k = i_x(k,3) - i_x(k,2) \\ \Delta i_x|S_c^k = i_x(k,4) - i_x(k,3) \\ \Delta i_x|S_d^k = i_x(k+1,1) - i_x(k,4) \end{cases}. \tag{27}$$

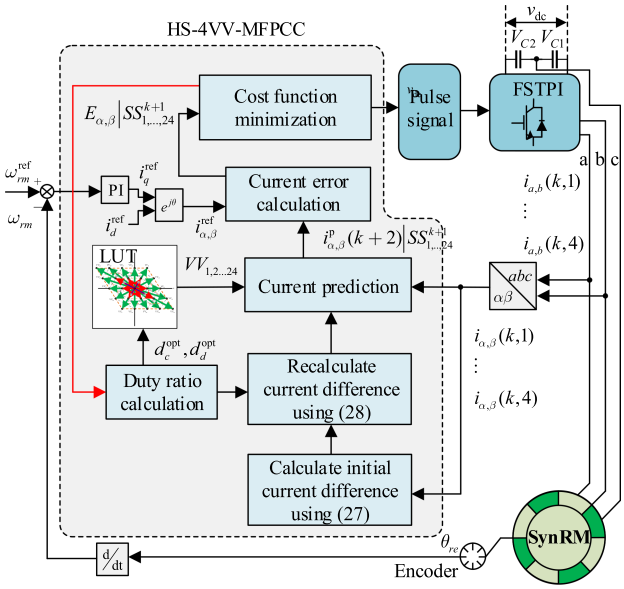

FIGURE 6. Control diagram of HS-4VV-MFPCC.

The equivalent current difference equation in (27) can be expressed relative to HS by integrating the calculated optimal duty ratios of d_c^{opt} and d_d^{opt}. The resulting expression is given as follows:

$$\begin{aligned} \Delta i_x^{\text{opt}}|SS_n^k = {} & 0.25\Delta i_x|S_a^k + 0.25\Delta i_x|S_b^k \\ & + d_c^{\text{opt}} \cdot \Delta i_x|S_c^k \\ & + \left(0.50 - d_c^{\text{opt}}\right) \cdot \Delta i_x|S_d^k. \end{aligned} \tag{28}$$

Similarly, by extending the current difference calculation to the $[k+1]$th sampling period, the optimal current difference component $\Delta i_x^{\text{opt}}|SS_n^k$ is obtainable as follows:

$$\begin{aligned} \Delta i_x^{\text{opt}}|SS_n^{k+1} = {} & 0.25\Delta i_x|S_a^{k+1} + 0.25\Delta i_x|S_b^{k+1} \\ & + d_c^{\text{opt}} \cdot \Delta i_x|S_c^{k+1} \\ & + \left(0.50 - d_c^{\text{opt}}\right) \cdot \Delta i_x|S_d^{k+1}. \end{aligned} \tag{29}$$

Combining (28) and (29), the current prediction equation due to the switching mode SS_n^{k+1} can be described as follows:

$$i_x^{\text{p}}(k+2)|SS_n^{k+1} = i_x(k,1) + \Delta i_x^{\text{opt}}|SS_n^k + \Delta i_x^{\text{opt}}|SS_n^{k+1}. \tag{30}$$

Finally, the cost function can be calculated based on the current error calculation defined in (20) and expressed accordingly as follows:

$$G|SS_n^{k+1} = \left(i_x^{\text{ref}} - i_x^{\text{p}}(k+2)|SS_n^{k+1}\right)^2. \tag{31}$$

The optimal duty ratios can be solved by following the strategy defined in (23)–(26). In summary, a block diagram of the HS-4VV-MFPCC is shown in Fig. 6. The process workflow is detailed in Fig. 7.

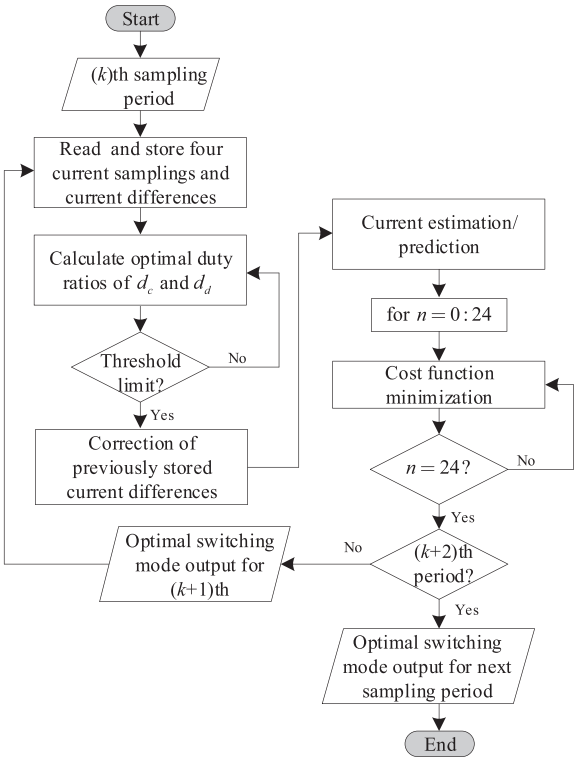

FIGURE 7. Simplified workflow process of the HS-4VV-MFPCC.

TABLE 2. Parameter of Simulations

Parameter	Unit	Value
Number of poles	pole	4
Rated power	W	500
Stator resistance	Ω	2.5
d-axis inductance	mH	48
q-axis inductance	mH	24.5
Rotational inertia	kg·m^2	0.0183
Friction of coefficient	N·m·s/rad	0.0063
Leakage inductance	mH	10
dc-link voltage	V	300
Maximum rated speed	r/min	1500
Sampling time	μs	100

V. PRELIMINARY VALIDATION BY SIMULATIONS

The performance of the proposed control method under model-based and model-free schemes, known as HS-4VV-MBPCC and HS-4VV-MFPCC, respectively, is first investigated in this section using MATLAB/Simulink. Table 2 lists the simulation parameters employed in both predictive methods to facilitate fair comparison.

Variations in the inductive parameter are only examined for parameter mismatch conditions because they are known to have a more significant impact on predictive controllers than variations in the resistive parameter [32]. The variations are set under two conditions: a 50% decrease and a 200% increase relative to the nameplate value. Since the gains of the proportional integral (PI)-based speed controller are fixed in the simulations, the corresponding q-axis current commands will vary as the motor parameters are changed.

Figs. 8 and 9 show the comparative α–β current response of HS-4VV-MBPCC and HS-4VV-MFPCC, respectively. It can be observed under the model-based predictive scheme

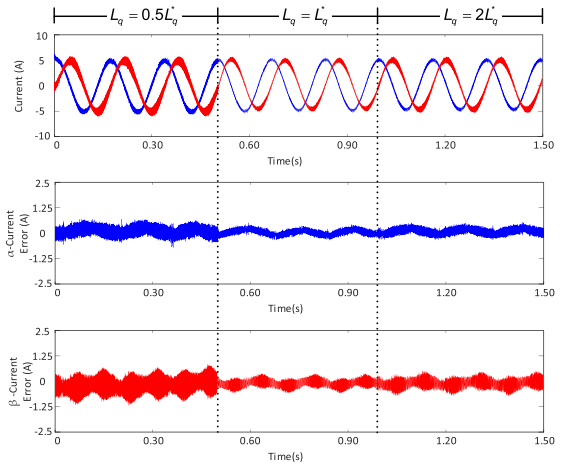

FIGURE 8. Performance of HS-4VV-MBPCC under inductance variations.

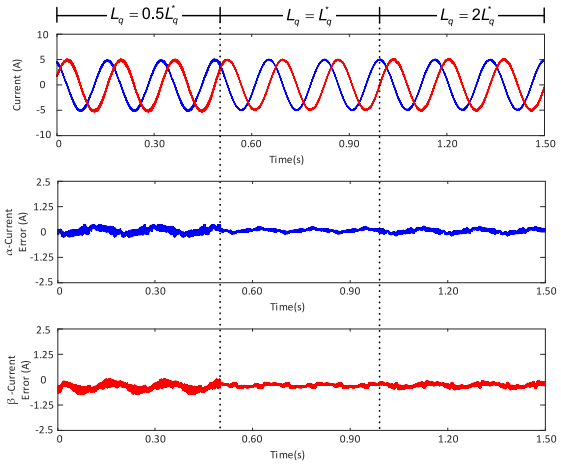

FIGURE 9. Performance of HS-4VV-MFPCC under inductance variations.

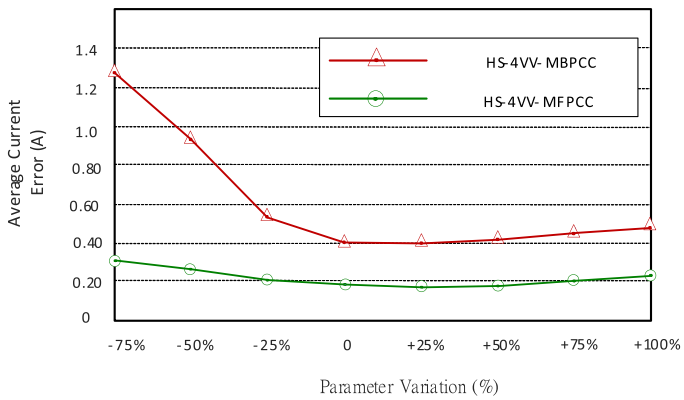

FIGURE 10. Average current error curve under inductance variations.

TABLE 3. SynRM Specifications

Parameter	Unit	Value
Number of poles	pole	4
Rated power	W	500
Rated torque	N·m	2
Rated speed	r/min	1500
Stator resistance	Ω	2.5
d-axis inductance	*m*H	48
q-axis inductance	*m*H	24.5

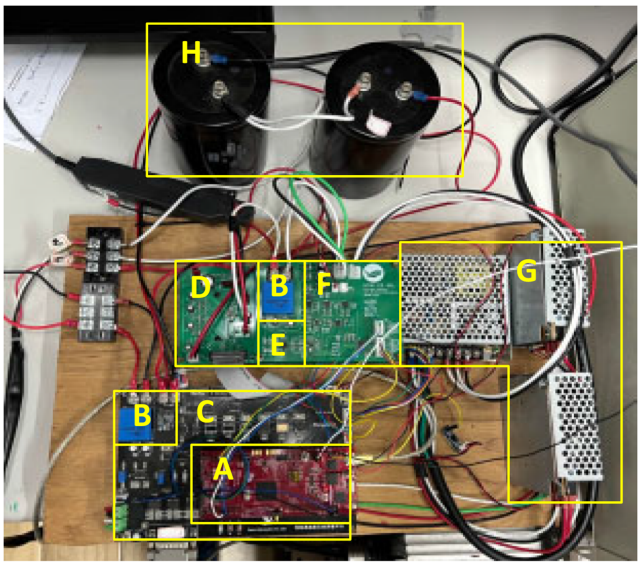

(a)

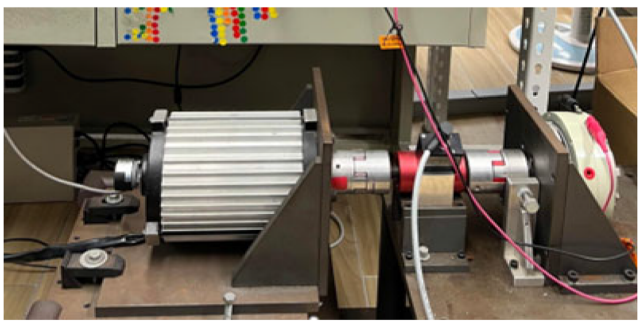

(b)

FIGURE 11. Experimental test bench. (a) Drive circuit board. (b) Motor load.

that parameter variation primarily affects the current response of the controller with large current ripples. The influence of parameter mismatch is predominantly observed under the reduced condition of inductive parameter, where a heavier build-up of current ripples is noticeable. When the parameter value is increased by 200%, a slight change can be observed

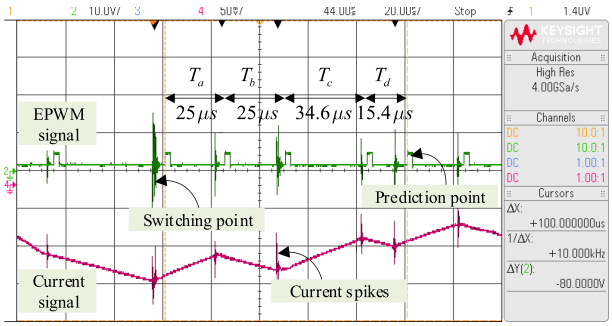

FIGURE 12. Switching signals of the applied four voltage vectors derived from the oscilloscope.

compared to the ideal setting. The findings suggest that the inductive parameter severely impacts prediction accuracy when it is decreased relative to its nominal value. For HS-4VV-MFPCC, shown in Fig. 9, it is evident that current ripples are less affected by parameter variations. The model-free method takes advantage of insensitivity to any changes in the motor parameters. At a 50% decrease, the current ripples are seen to increase slightly because of the PI-based speed controller. However, the increase is considered insignificant compared to the model-based controller. The summary of the current response between −75% and +100% variations in the inductive parameters is shown in Fig. 10. Furthermore, simulation results are presented as an initial proof of concept for the proposed method. It should be expected that minimal discrepancy in results can be observed compared to the hardware implementation as simulation works are demonstrated in an almost perfect setup. More realistic and practical results can be observed in experimental validations.

VI. EXPERIMENTAL EVALUATIONS

A. HARDWARE AND TEST BENCH

Illustrated in Fig. 11 is the experimental setup to perform the tests. In Fig. 11(a), the drive circuit board consists of the following subcomponents: (A) a digital signal processor of TMS320F28379D microcontroller from Texas Instruments, Inc., (B) current sensors of LA25-NP type, (C) overcurrent current protection board with built-in circuit encoder, (D) power module inverter (SCM1246MF), (E) ADA4940, (F) AD4001, (G) power source, and (H) pair of capacitors rated 400 V/10 000 μF. Fig. 11(b) depicts the motor load SynRM coupled with an external load torque device. The motor specifications are listed in Table 3.

B. VALIDATION OF HYBRID SWITCHING OF SYNTHESIZED VOLTAGE VECTORS

Fig. 12 demonstrates the HS mechanism of four input voltage vectors obtained from an oscilloscope. The switching response of the inverter corresponding to the four applied voltage vectors in one sampling period is configured by the controller's enhanced pulsewidth modulator. The sampling time is set to 100 μs. The adaptivity of the HS control can be

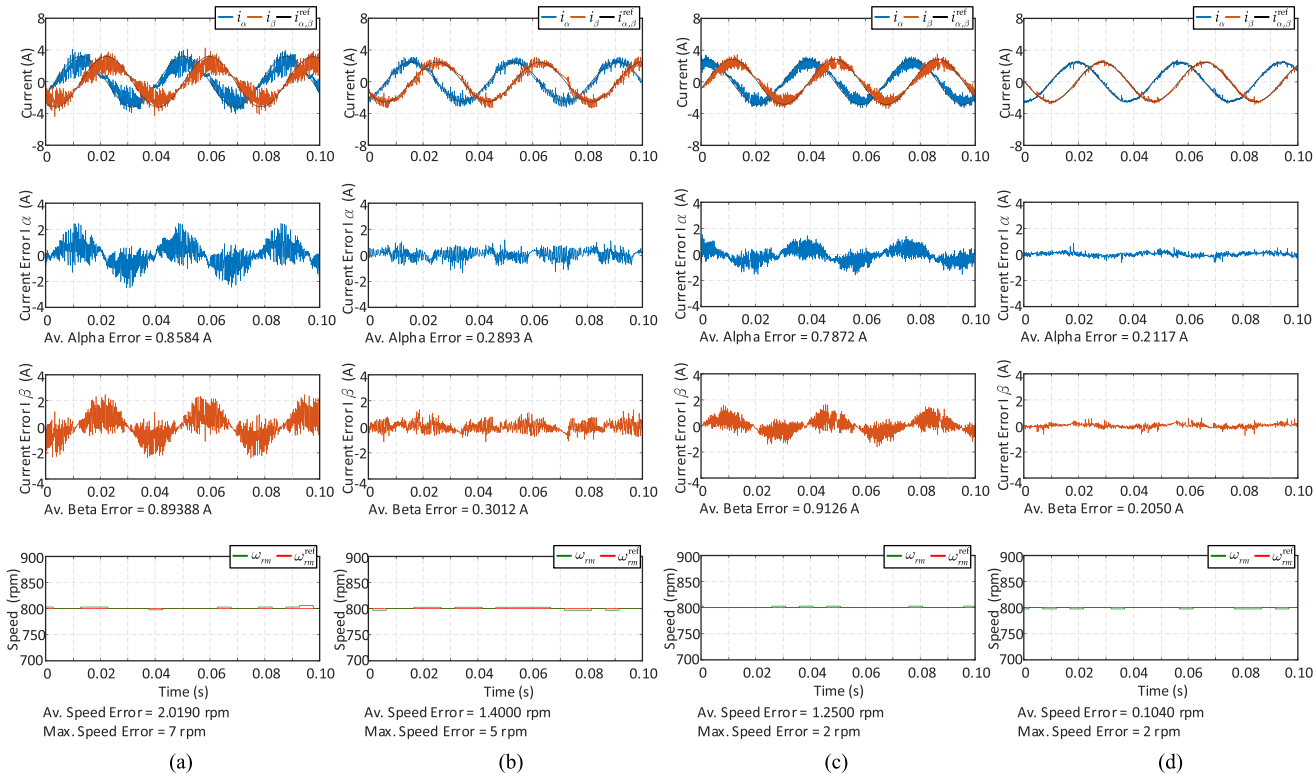

FIGURE 13. **Steady-state current response at a speed command of 800 r/min and a load torque of 1.5 N·m. In each subfigure from top to bottom: α–β current waveforms, α-phase current error, β-phase current error, and speed tracking performance. (a) C-MBPCC. (b) C-MFPCC. (c) HS-4VV-MBPCC. (d) HS-4VV-MFPCC.**

TABLE 4. **Execution Time of Different MPCC Algorithms**

Algorithms	Sampling time	Execution time
C-MBPCC	100 μs	13.3 μs
C-MFPCC	100 μs	15.4 μs
HS-4VV-MBPCC	100 μs	39.4 μs
HS-4VV-MFPCC	100 μs	43.5 μs

observed from the applied durations of the four input voltage vectors. At any instant, it is noticeable that the first half of the sampling duration actuates twice at a fixed period of 25 μs each, denoted by T_a and T_b. The last half registers variable switching durations marked as T_c and T_d, at 34.6 and 15.4 μs, respectively.

C. EXECUTION TIME EVALUATION

The execution time of the TMS320F28379D DSP under various MPCC algorithms is experimentally measured to determine their respective computational efficiencies. Four sets of predictive controllers are evaluated, including the conventional MBPCC (C-MBPCC), conventional MFPCC (C-MFPCC), and proposed methods of HS-4VV-MBPCC and HS-4VV-MFPCC. Table 4 shows that C-MBPCC and C-MFPCC have the shortest execution time because of only four candidate voltage vectors to optimize. As the admissible voltage vector increases, a significant increase can be noticed in the case of HS-4VV-MBPCC and HS-4VV-MFPCC. In particular, the HS-4VV-MFPCC has the longest time of 43.5 μs or almost double that of its conventional counterpart. However, given that the sampling design for the controllers is 100 μs, the performance of the proposed control methods remains practical and viable.

D. STEADY-STATE EXPERIMENTAL RESULTS

In evaluating the performance of the proposed method over the conventional predictive schemes, the steady-state result is presented under conditions of speed and current commands. Fig. 13 illustrates the stator current response at a speed command of 800 r/min with an external load torque of 1.5 N·m. Fig. 14, on the other hand, shows current waveforms at a current command of 6A, operating at a speed frequency of 30 Hz. Both figures show experimental results of α-phase and β-phase current errors, with speed tracking performance shown in Fig. 13.

The following has been observed based on the steady-state experimental results.

1) The proposed HS-4VV-MFPCC yields the most efficient current tracking performance based on the average ripples and errors recorded. The C-MBPCC generates the highest average current error, whereas the HS-4VV-MFPCC yields the lowest,

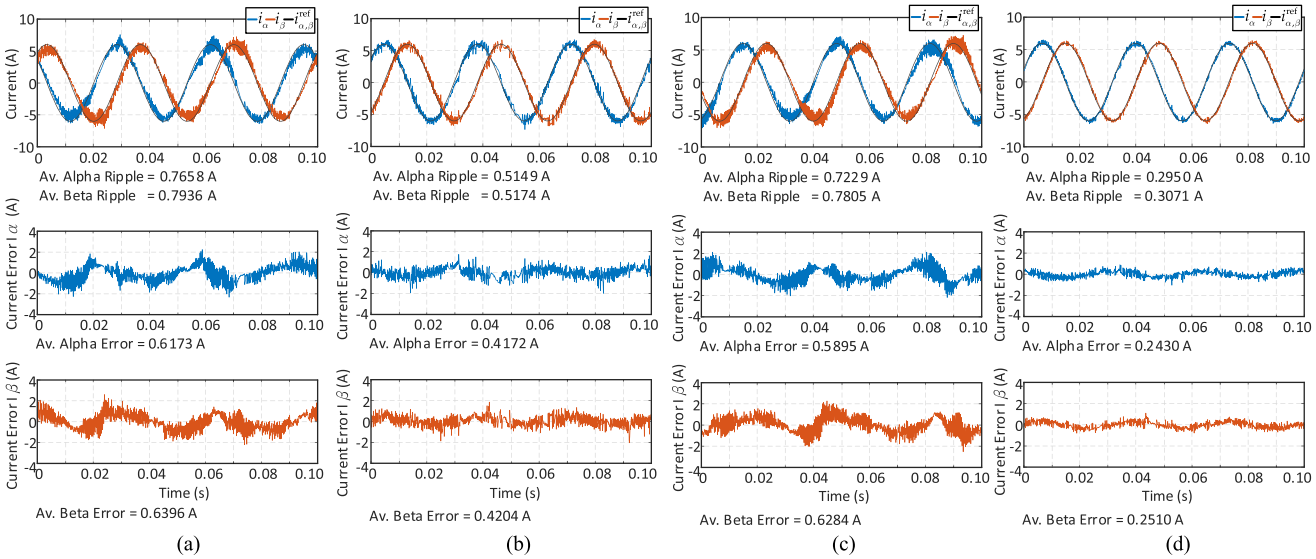

FIGURE 14. Steady-state current response at a current command of 6 A and a frequency of 30 Hz. In each subfigure from top to bottom: $\alpha-\beta$ current waveforms, α-phase current error, and β-phase current error. (a) C-MBPCC. (b) C-MFPCC. (c) HS-4VV-MBPCC. (d) HS-4VV-MFPCC.

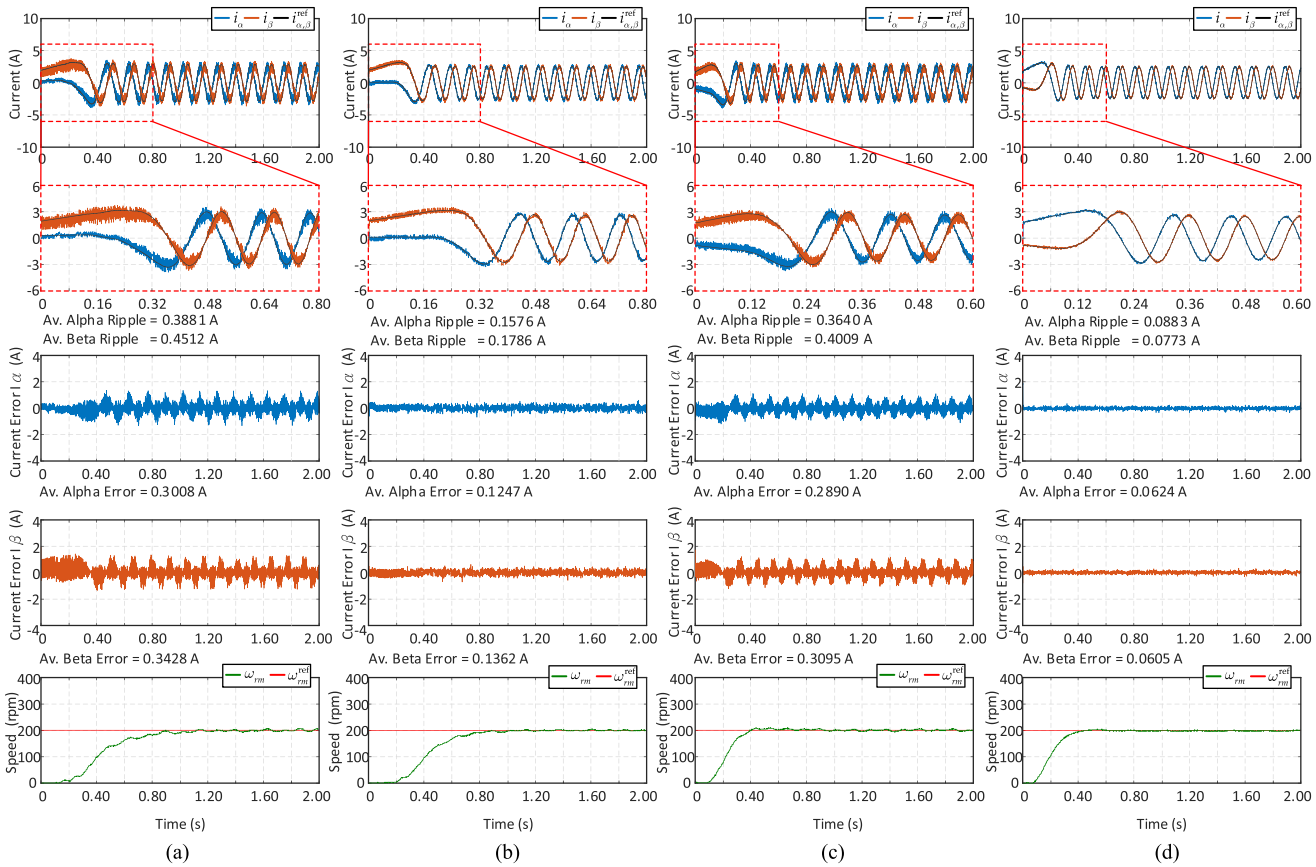

FIGURE 15. Dynamic response from a standstill to a speed command of 200 r/min and a load torque of 1.5 N·m. In each subfigure from top to bottom: $\alpha-\beta$ current waveforms, magnified view of $\alpha-\beta$ current waveforms, α-phase current error, β-phase current error, and speed tracking performance. (a) C-MBPCC. (b) C-MFPCC. (c) HS-4VV-MBPCC. (d) HS-4VV-MFPCC.

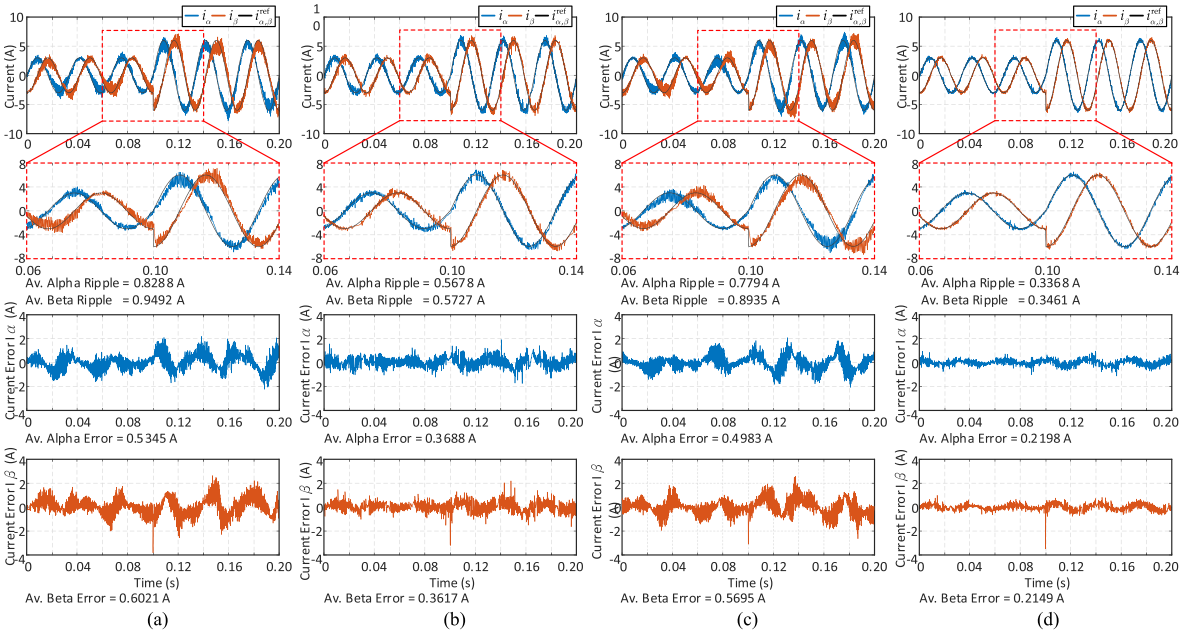

FIGURE 16. **Dynamic response under a current step command from 3 to 6A, operating at a 30 Hz frequency. In each subfigure from top to bottom: α–β current waveforms, magnified view of α–β current waveforms, α-phase current error, and β-phase current error. (a) C-MBPCC. (b) C-MFPCC. (c) HS-4VV-MBPCC. (d) HS-4VV-MFPCC.**

implying error reductions of 76.18 % and 60.70% for Figs. 13 and 14, respectively.

2) The model-free schemes, C-MFPCC and HS-4VV-MFPCC, outperform their model-based counterparts, which indicates that they effectively suppress parameter mismatch and uncertainty.

3) The speed tracking performance is also significantly improved using the proposed method, with a speed deviation of 0.1040 r/min compared to 2.0190 r/min in the conventional model-based predictive scheme.

E. DYNAMIC EXPERIMENTAL RESULTS

Various tests are performed to evaluate the dynamic response of the MPCC algorithms, including a speed step command from a standstill condition to the desired speed command, a current step command, and an on-load and off-load torque injection. The dynamic responses of speed and current step commands are shown in Figs. 15 and 16. Similarly, Fig. 17 displays the dynamic experimental waveforms of stator currents in α–β, the equivalent error response, d–q current waveforms, and the transient speed tracking. The dynamic setting is carried out at a constant speed command of 800 r/min with on- and off-load injection of 1.5 N·m external torque. Based on the current ripples seen on each MPCC algorithm from Fig. 17(a)–(d), it is evident that the proposed method produces the most significant current dynamic output. From these three conditions performed, C-MBPCC and HS-4VV-MBPCC perform the worst, owing to their model-based characteristics. In contrast, the application of four input voltage vectors of HS-4VV-MFPCC has contributed to better iterations and predictions of current samplings, resulting in a better quality of current waveforms illustrated in the experimental results.

TABLE 5. **Quantitative Summary of %THD*i* Comparison**

Figure no.	C-MBPCC	C-MFPCC	HS-4VV-MBPCC	HS-4VV-MFPCC
13	12.34	11.76	10.53	9.81
14	4.99	4.52	2.15	1.77
15	6.15	5.86	2.94	2.12
16	5.39	5.28	5.34	4.17
17	13.27	12.13	9.68	7.89

F. TOTAL HARMONIC DISTORTION RESULTS

The harmonic profile of the different tests performed is illustrated in this section. The current total harmonic distortion (THD*i*) expressed in percentage (%) is used to assess the performance of the proposed controller. The lower theTHD*i* implies better performance with lesser induced heat, lower electromagnetic emissions, and lesser core loss in the machine. The quantitative summary of the test performed from Figs. 13–17 is described in Table 5. Results show that the proposed HS-4VV-MFPCC can significantly mitigate the effect of harmonic distortion in the SynRM regardless of operating conditions. The highest recorded THD*i* is observed under operating conditions of high external load torque of 1.5 N·m in Figs. 13 and 17. Under the current control scheme shown in Figs. 14 and 16, it can be observed that the proposed method can reduce the harmonics by 17.67% and 21.03%,

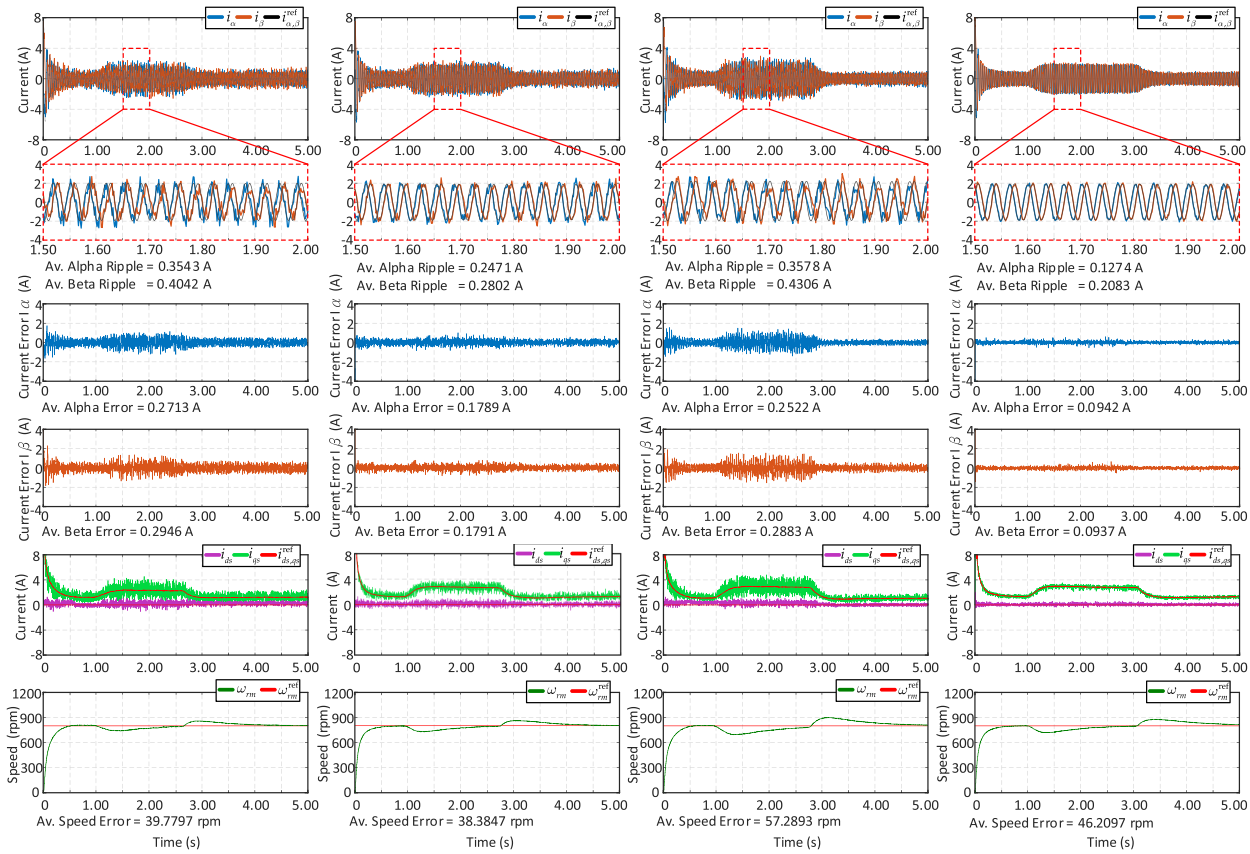

FIGURE 17. **Dynamic response from a standstill (at rest) to 800 r/min with a sudden on-load and off-load torque injection of 1.5 Nm. In each subfigure from top to bottom: α–β current waveforms, magnified view of α–β current waveforms, α-phase current error, β-phase current error, stator currents in d–q axis, and speed tracking performance. (a) C-MBPCC. (b) C-MFPCC. (c) HS-4VV-MBPCC. (d) HS-4VV-MFPCC.**

respectively, when compared with HS-4VV-MBPCC. Meanwhile, compared with the traditional MFPCC, the reduction is 60.84% and 21.03%.

VII. CONCLUSION

An integrated MFPCC based on the HS mechanism of four voltage vectors is presented in this article. The control duration of switching voltage vectors is designed to be fixed and variable through HS. Moreover, 24 new synthesized voltage vectors denoted as switching modes are created through linear expansions of the space vector plane to boost the number of candidate selections. Validation of the control performance of the proposed method is demonstrated under various settings, such as parameter mismatch tests, speed commands under different load torque conditions, and current commands. Simulation and experimental results show that the proposed HS-4VV-MFPCC can successfully improve current prediction accuracy thanks to the increased iteration calculations of current differences. An average reduction in current ripple and current error is observed by more than 50%, and substantial improvements in current THDi by an average of 42% when compared to conventional MBPCC.

REFERENCES

[1] K. Shenai, P. G. Neudeck, and G. Schwarze, "Design and technology of compact high-power converters," *IEEE Aerosp. Electron. Syst. Mag.*, vol. 16, no. 3, pp. 27–31, Mar. 2001, doi: 10.1109/62.911318.

[2] T. J. Blalock, "The rotary era, part 1: Early AC-to-DC power conversion," *IEEE Power Energy Mag.*, vol. 11, no. 5, pp. 82–92, Sep./Oct. 2013, doi: 10.1109/MPE.2013.2265791.

[3] A. Hughes and B. Drury, "Synchronous and brushless permanent magnet machines and drives," in *Electric Motor and Drives: Fundamental, Types and Applications*, 4th ed. Amsterdam, The Netherlands: Elsevier, 2013, pp. 281–313, doi: 10.1016/C2011-0-07555-5.

[4] C. A. Agustin, J. T. Yu, C. K. Lin, and X. Y. Fu, "A modulated model predictive current controller for interior permanent-magnet synchronous motors," *Energies*, vol. 12, no. 15, Jul. 2019, Art. no. 2885, doi: 10.3390/en12152885.

[5] S. W. Su, C. M. Hackl, and R. Kennel, "Analytical prototype functions for flux linkage approximation in synchronous machines," *IEEE Open J. Ind. Electron. Soc.*, vol. 3, pp. 265–282, 2022, doi: 10.1109/OJIES.2022.3162336.

[6] J. Kolehmainen, "Synchronous reluctance motor with form blocked rotor," *IEEE Trans. Energy Convers.*, vol. 25, no. 2, pp. 450–456, Jun. 2010, doi: 10.1109/TEC.2009.2038579.

[7] S. Taghavi and P. Pillay, "A sizing methodology of the synchronous reluctance motor for traction applications," *IEEE J. Emerg. Sel. Topics Power Electron.*, vol. 2, no. 2, pp. 329–340, Jun. 2014, doi: 10.1109/JESTPE.2014.2299235.

[8] D. Zhou, J. Zhao, and Y. Liu, "Predictive torque control scheme for three-phase four-switch inverter-fed induction motor drives with DC-link voltages offset suppression," *IEEE Trans. Power Electron.*, vol. 30, no. 6, pp. 3309–3318, Jun. 2015, doi: 10.1109/TPEL.2014.2338395.

[9] C. K. Lin, C. A. Agustin, J. T. Yu, Y. S. Cheng, F. M. Chen, and Y. S. Lai, "A modulated model-free predictive current control for four-switch three-phase inverter-fed SynRM drive systems," *IEEE Access*, vol. 9, pp. 162984–162995, 2021, doi: 10.1109/ACCESS.2021.3133023.
[10] S. Dasgupta, S. N. Mohan, S. K. Sahoo, and S. K. Panda, "Application of four-switch-based three-phase grid-connected inverter to connect renewable energy source to a generalized unbalanced microgrid system," *IEEE Trans. Ind. Electron.*, vol. 60, no. 3, pp. 1204–1215, Mar. 2013, doi: 10.1109/TIE.2012.2202350.
[11] X. Tan, Q. Li, H. Wang, L. Cao, and S. Han, "Variable parameter pulse width modulation-based current tracking technology applied to four switch three-phase shunt active power filter," *IET Power Electron.*, vol. 6, no. 3, pp. 543–553, Mar. 2013, doi: 10.1049/iet-pel.2012.0503.
[12] X. Zang and G. H. B. Foo, "Over-modulation of constant switching frequency-based DTC for reluctance synchronous motors incorporating field-weakening operation," *IEEE Trans. Ind. Electron.*, vol. 66, no. 1, pp. 37–47, 2018, doi: 10.1109/TIE.2018.2826478.
[13] D. Casadei, F. Profumo, G. Serra, and A. Tani, "FOC and DTC: Two viable schemes for induction motors torque control," *IEEE Trans. Power Electron.*, vol. 17, no. 5, pp. 779–787, Sep. 2002, doi: 10.1109/TPEL.2002.802183.
[14] M. P. Kazmierkowski, R. Krishnan, and F. Blaabjerg, "Control of PWM inverter-fed induction motors," in *Control in Power Electronics: A Volume in Academic Press Series in Engineering*. Amsterdam, The Netherlands: Elsevier, 2003, pp. 161–207, doi: 10.1016/B978-012402772-5/50006-5.
[15] H. Hadla and F. Santos, "Performance comparison of field-oriented control, direct torque control, and model-predictive control for SynRMs," *Chin. J. Elect. Eng.*, vol. 8, no. 1, pp. 24–37, Mar. 2022, doi: 10.23919/CJEE.2022.000003.
[16] R. Baidya et al., "Enabling multistep model predictive control for transient operation of power converters," *IEEE Open J. Ind. Electron. Soc.*, vol. 1, pp. 284–297, 2020, doi: 10.1109/OJIES.2020.3029358.
[17] D. F. Valencia, R. Tarvirdilu-Asl, C. Garcia, J. Rodriguez, and A. Emadi, "A review of predictive control techniques for switched reluctance machine drives. Part I: Fundamentals and current control," *IEEE Trans. Energy Convers.*, vol. 36, no. 2, pp. 1313–1322, Jun. 2021, doi: 10.1109/TEC.2020.3047983.
[18] Y. Zhou, H. Li, R. Liu, and J. Mao, "Continuous voltage vector model-free predictive current control of surface mounted permanent magnet synchronous motor," *IEEE Trans. Energy Convers.*, vol. 34, no. 2, pp. 899–908, Jun. 2019, doi: 10.1109/TEC.2018.2867218.
[19] W. Tu, G. Luo, R. Zhang, Z. Chen, and R. Kennel, "Finite-control-set model predictive current control for PMSM using grey prediction," in *Proc. IEEE Energy Convers. Congr. Expo.*, 2016, pp. 1–7, doi: 10.1109/ECCE.2016.7855117.
[20] X. Zhang, B. Hou, and Y. Mei, "Deadbeat predictive current control of permanent-magnet synchronous motors with stator current and disturbance observer," *IEEE Trans. Power Electron.*, vol. 32, no. 5, pp. 3818–3834, May 2017, doi: 10.1109/TPEL.2016.2592534.
[21] H. T. Nguyen and J. W. Jung, "Finite control set model predictive control to guarantee stability and robustness for surface-mounted PM synchronous motors," *IEEE Trans. Ind. Electron.*, vol. 65, no. 11, pp. 8510–8519, Nov. 2018, doi: 10.1109/TIE.2018.2814006.
[22] J. Rodriguez et al., "Latest advances of model predictive control in electrical drives—Part I: Basic concepts and advanced strategies," *IEEE Trans. Power Electron.*, vol. 37, no. 4, pp. 3927–3942, Apr. 2022, doi: 10.1109/TPEL.2021.3121532.
[23] X. Li, S. Zhang, C. Zhang, Y. Zhou, and C. Zhang, "An improved deadbeat predictive current control scheme for open-winding permanent magnet synchronous motors drives with disturbance observer," *IEEE Trans. Power Electron.*, vol. 36, no. 4, pp. 4622–4632, Apr. 2021, doi: 10.1109/TPEL.2020.3024227.
[24] L. He, F. Wang, J. Wang, and J. Rodríguez, "Zynq implemented Luenberger disturbance observer based predictive control scheme for PMSM drives," *IEEE Trans. Power Electron.*, vol. 35, no. 2, pp. 1770–1778, Feb. 2020, doi: 10.1109/TPEL.2019.2920439.
[25] R. Yang, M. Y. Wang, L. Y. Li, C. M. Zhang, and J. L. Jiang, "Robust predictive current control with variable-gain adaptive disturbance observer for PMLSM," *IEEE Access*, vol. 6, pp. 13158–13169, 2018, doi: 10.1109/ACCESS.2018.2809608.
[26] L. Yan and X. Song, "Design and implementation of Luenberger model-based predictive torque control of induction machine for robustness improvement," *IEEE Trans. Power Electron.*, vol. 35, no. 3, pp. 2257–2262, Mar. 2020, doi: 10.1109/TPEL.2019.2939283.
[27] M. Fliess and C. Join, "Model-free control and intelligent PID controllers: Towards a possible trivialization of nonlinear control?," *IFAC Proc. Volumes*, vol. 42, no. 10, pp. 1531–1550, 2009, doi: 10.3182/20090706-3-FR-2004.00256.
[28] C. K. Lin, T. H. Liu, J. T. Yu, L. C. Fu, and C. F. Hsiao, "Model-free predictive current control for interior permanent-magnet synchronous motor drives based on current difference detection technique," *IEEE Trans. Ind. Electron.*, vol. 61, no. 2, pp. 667–681, Feb. 2014, doi: 10.1109/TIE.2013.2253065.
[29] Y. Zhang, J. Jin, and L. Huang, "Model-free predictive current control of PMSM drives based on extended state observer using ultralocal model," *IEEE Trans. Ind. Electron.*, vol. 68, no. 2, pp. 993–1003, Feb. 2021, doi: 10.1109/TIE.2020.2970660.
[30] C. A. Agustin, J. T. Yu, C. K. Lin, J. Jai, and Y. S. Lai, "Triple-voltage-vector model-free predictive current control for four-switch three-phase inverter-fed SPMSM based on discrete-space-vector modulation," *IEEE Access*, vol. 9, pp. 60352–60363, 2021, doi: 10.1109/ACCESS.2021.3074067.
[31] C. Xiong, H. Xu, T. Guan, and P. Zhou, "A constant switching frequency multiple-vector-based model predictive current control of five-phase PMSM with nonsinusoidal back EMF," *IEEE Trans. Ind. Electron.*, vol. 67, no. 3, pp. 1695–1707, Mar. 2020, doi: 10.1109/TIE.2019.2907502.
[32] M. Khalilzadeh, S. Vaez-Zadeh, J. Rodriguez, and R. Heydari, "Model-free predictive control of motor drives and power converters: A review," *IEEE Access*, vol. 9, pp. 105733–105747, 2021, doi: 10.1109/ACCESS.2021.3098946.
[33] X. Yuan, Y. Zuo, Y. Fan, and C. H. T. Lee, "Model-free predictive current control of SPMSM drives using extended state observer," *IEEE Trans. Ind. Electron.*, vol. 69, no. 7, pp. 6540–6550, Jul. 2022, doi: 10.1109/TIE.2021.3095816.

CHENG-KAI LIN was born in Taipei, Taiwan, in 1980. He received the B.S. degree in electrical engineering from the Ming Chi University of Technology, Taipei, Taiwan, in 2002, and the M.S. and Ph.D. degrees in electrical engineering from the National Taiwan University of Science and Technology, Taipei, Taiwan, in 2004 and 2009, respectively.

From October 2009 to August 2012, he was a Postdoctoral Researcher with the Department of Electrical Engineering, National Taiwan University, Taipei, Taiwan. He is currently an Associate Professor of electrical engineering with National Taiwan Ocean University, Keelung, Taiwan. His research interests include motor drive control, power electronic applications, and control applications.

CRESTIAN A. AGUSTIN was born in Isabela, Philippines, in 1989. He received the B.S. degree in electrical engineering from Isabela State University, Ilagan, Philippines, in 2012, the M.S. degree in engineering management from the University of La Salette, Santiago City, Philippines, in 2015, the M.S. in electrical engineering from the University of St. Louis, Cagayan, Philippines, in 2017, and the Ph.D. degree in electrical engineering from National Taiwan Ocean University, Keelung City, Taiwan, in 2022.

From 2014 to 2017, he was a Resident Engineer with the SM Engineering Design and Development, Pasay City, Philippines. He is currently a Lecturer with Electrical Engineering Department, Isabela State University. His research interests include control of motor drives and inverter topologies.